

**Using tracer observations to reduce the uncertainty of ocean diapycnal mixing and climate  
- carbon cycle projections**

Andreas Schmittner\*, College of Oceanic and Atmospheric Sciences, Oregon State University,  
Corvallis, OR, U.S.A.

Nathan M. Urban, Department of Geosciences, The Pennsylvania State University, University  
Park, PA, U.S.A.

Klaus Keller, Department of Geosciences, The Pennsylvania State University, University Park,  
PA, U.S.A.

Damon Matthews, Department of Geography, Planning and Environment, Concordia University,  
Montreal, Quebec, Canada

\* Corresponding author. 104 COAS Admin Bldg, Corvallis, Oregon 97331-5503, phone 541 737  
9952, fax 541 737 2064, [aschmitt@coas.oregonstate.edu](mailto:aschmitt@coas.oregonstate.edu)

Index terms: 3245, 1615, 3275, 0428

Submitted to *Global Biogeochemical Cycles*

Friday, November 07, 2008

## Abstract

What is the uncertainty of climate-carbon cycle projections in response to anthropogenic greenhouse gas emissions and how can we reduce this uncertainty? We address this question by quantifying the ability of available ocean tracer observations to constrain the values of diapycnal diffusivity in the pelagic ocean ( $K_v$ ), a key uncertain parameter representing sub-gridscale diapycnal (vertical) mixing in physical circulation models. We show that model versions with weak mixing lead to higher projections of atmospheric  $\text{CO}_2$  and larger global warming than models with vigorous mixing. Slower heat uptake as well as slower carbon uptake by the oceans contribute about equally to the accelerated warming in the low mixing models. A Bayesian data-model fusion method is developed to quantify the likelihood of different structural and parametric model choices given an array of observed 20th century ocean tracer distributions. These spatially resolved observations provide strong limits on the upper value of  $K_v$ , whereas global metrics used in previous studies, such as the historical evolution of global average surface air temperature, global ocean heat uptake, or atmospheric  $\text{CO}_2$  concentration, provide only poor constraints. We compare different methods to quantify the probability of a particular  $K_v$  value given the observational constraints. One-dimensional (horizontally averaged) data result in sharper probability density functions compared with the full 3D fields. This unexpected result opens an avenue to objectively determine the optimal degree of aggregation at which model predictions have skill, and at which observations are most helpful in constraining model parameters. Our best estimate for  $K_v$  in the pelagic pycnocline is around  $0.05\text{-}0.2\text{ cm}^2/\text{s}$ , in agreement with earlier independent estimates based on tracer dispersion experiments and turbulence microstructure measurements.

## 1. Introduction

Atmospheric CO<sub>2</sub> concentrations are rising faster than ever since continuous monitoring began in 1959 [Canadell *et al.*, 2007]. Increasing anthropogenic carbon emissions is the main cause of this accelerating growth, but reduced uptake of atmospheric CO<sub>2</sub> by ocean [Le Quere *et al.*, 2007] and land are also hypothesized to play a role [Canadell *et al.*, 2007]. These observations are consistent with previous coupled climate-carbon cycle model simulations that predict decreases in terrestrial and oceanic carbon uptake in the future due to changes in climate [Cox *et al.*, 2000; Dufresne *et al.*, 2002; Friedlingstein *et al.*, 2006; Govindasamy *et al.*, 2005; Jones *et al.*, 2003; Joos *et al.*, 1999; Joos *et al.*, 2001; Matear and Hirst, 1999; Matthews *et al.*, 2005b; Sarmiento *et al.*, 1998; Zeng *et al.*, 2004]. However, the Coupled Climate - Carbon Cycle Model Intercomparison Project (C<sup>4</sup>MIP) [Friedlingstein *et al.*, 2006] shows a large range in the projected magnitude of this feedback between different models. Projected atmospheric CO<sub>2</sub> levels for emission scenario SRES A2 at year 2100 range from ~700 ppmv to ~1000 ppmv, and up to 200 ppmv of this difference can be attributed to differences in the climate-carbon cycle feedback [Friedlingstein *et al.*, 2006]. Thus, the unknown magnitude and uncertainty of the future climate-carbon cycle feedback presents a major hindrance in the assessment of the impacts of carbon emission scenarios.

The reasons for the aforementioned model differences are poorly understood. Although the C<sup>4</sup>MIP models showed larger differences in land uptake (-6 to +10 GtC/yr), there were also considerable differences in ocean uptake (+4 to +10 GtC/yr) by the year 2100 [Friedlingstein *et al.*, 2006]. Matthews *et al.* [2005a] shows that differences in the parameterizations of the dependency of terrestrial vegetation growth rates on ambient temperatures have a large effect on carbon uptake on land in future warming experiments, suggesting that this might be a major contributor to the uncertainty range observed in the C<sup>4</sup>MIP models. Even less is known about reasons for the differences in ocean uptake, although more simplified models (either in terms of physics or biology) apparently show a larger sensitivity of carbon uptake with respect to temperature changes than more complex models [Friedlingstein *et al.*, 2006]. A more detailed comparison between two specific models attributes a two fold difference in oceanic carbon uptake (4 GtC/yr in the UK Hadley Center model versus 8 GtC/yr in the French IPSL model at

700 ppmv atmospheric CO<sub>2</sub>) due to increasing CO<sub>2</sub> alone (without climate change) to differences in Southern Ocean circulation [*Friedlingstein et al.*, 2003].

The models included in the C<sup>4</sup>MIP exercise are very heterogeneous and range from box models via zonally averaged and slab mixed layer ocean models to fully three-dimensional coupled ocean-atmosphere general circulation models (GCMs). However, these studies are mostly silent on the question of how probable the different model structures are given the available observational constraints. Since no systematic comparison with observations has been performed for the C<sup>4</sup>MIP models, it remains unclear whether or not the uncertainty range of the C<sup>4</sup>MIP models is realistic. It is very well possible that the model spread overestimates the true uncertainty if some models are inconsistent with observations, as is the case for the Ocean Carbon-cycle Model Intercomparison Project (OCMIP) models [*Doney et al.*, 2004; *Matsumoto et al.*, 2004].

It is also possible that the C<sup>4</sup>MIP models underestimate the true uncertainty, e.g. if the models do not represent a large enough range of unconstrained parameters. Recent Monte Carlo simulations with an atmosphere model suggest that model parameter uncertainties can increase the range of future climate projections considerably [*Murphy et al.*, 2004; *Stainforth et al.*, 2005]. A key uncertain parameter in ocean circulation models is the diapycnal (vertical) diffusivity  $K_v$ . The strong sensitivity of the global deep overturning circulation to  $K_v$  has been known since the pioneering study by *Bryan* [1987]. Here we investigate the uncertainty in ocean vertical mixing and its effect on future projections of climate and CO<sub>2</sub>.

Earlier studies show that tracer distributions in ocean models are sensitive to changes in ocean circulation and ventilation [*Doney et al.*, 2004; *England and Maier-Reimer*, 2001; *Gnanadesikan et al.*, 2004; *Matsumoto et al.*, 2004], but no attempt has been undertaken to quantify the probability of different model structures and parameters given spatially resolved observations of ocean tracer distributions. *Tomassini et al.* [2007] estimates probability density functions for multiple parameters, including  $K_v$ , of a simple climate model using global mean surface air temperature and global ocean heat content changes as observational constraints. That study finds the probability distribution for  $K_v$  is multimodal, and concludes that the globally averaged

metrics do not provide strong limits on the value of  $K_v$ . Here we show that multiple physical, geochemical and biogeochemical observations with spatial resolution can provide much stronger constraints on the diapycnal ocean diffusivity. The main goal of this paper, however, is to develop and demonstrate a Bayesian data-model fusion approach for spatially distributed tracer observations that can be used to assess and reduce the uncertainty of future climate projections.

## 2. Methods

### 2.1. Model

The UVic Earth System Climate Model [Weaver *et al.*, 2001] of intermediate complexity, includes a coarse resolution ( $1.8 \times 3.6^\circ$ , 19 vertical layers) three-dimensional general circulation model of the ocean. It has state-of-the-art physical parameterizations such as diffusive mixing along and across isopycnals, eddy induced tracer advection [Gent and McWilliams, 1990] and a scheme for the computation of tidally induced diapycnal mixing over rough topography [Simmons *et al.*, 2004]. In order to account for other sources of mixing, a globally constant background diffusivity  $K_{bg}$  is added to the tidally induced diffusivity  $K_v = K_{tidal} + K_{bg}$ . It is this background diffusivity  $K_{bg}$  that will be varied in our sensitivity study, from  $0.01 \text{ cm}^2/\text{s}$  to  $0.5 \text{ cm}^2/\text{s}$ . The tidally induced diffusivity rapidly decays in the water column above the sea floor with an exponential depth scale of 500 m. This results in the background diffusivity determining the value of diapycnal mixing in most parts of the pelagic pycnocline. Observations from the Southern Ocean show that diapycnal mixing is much larger than in other oceans [Naveira Garabato *et al.*, 2004]. We account for these observations by limiting  $K_v$  to  $\geq 1 \text{ cm}^2/\text{s}$  south of  $40^\circ\text{S}$ . Thus, the variations in  $K_{bg}$  affect mixing only in the open ocean north of  $40^\circ\text{S}$ .

A simple one-layer atmospheric energy-moisture balance model (EMBM) interactively calculates heat and water fluxes to ocean, land and sea ice, while wind velocities are prescribed from the NCAR/NCEP monthly climatology in the momentum transfer to the ocean and to a dynamic-thermodynamic sea ice model. The model does not use flux corrections. The model of the terrestrial vegetation and carbon cycle [Meissner *et al.*, 2003] is based on the Hadley Center model TRIFFID. The ocean biogeochemical model is based on the NPZD (nutrient, phytoplankton, zooplankton, detritus) ecosystem model of Schmittner *et al.* [2005b], and

includes a parameterization of fast nutrient recycling due to microbial activity after *Schartau and Oschlies* [2003]. It solves prognostic equations for two phytoplankton classes (nitrogen fixers and other phytoplankton) as well as for nitrate, phosphate, oxygen, dissolved inorganic carbon, alkalinity, radiocarbon and chlorofluorocarbons as tracers. The biogeochemical/carbon cycle model is described in detail in *Schmittner et al.* [2008]. Biological uptake and release occurs in fixed elemental ratios of carbon, phosphate, nitrate and oxygen. Calcium carbonate production is parameterized as a fixed ratio of the production of particulate organic matter in the water column. Remineralization of calcium carbonate is determined by instantaneous sinking with an e-folding depth of 3500 m.

The ensemble consists of 8 models with  $K_v=(0.01,0.05,0.1,0.15,0.2,0.3,0.4,0.5)$ . (In the following, for brevity, we omit the units of  $K_v$ , which are in  $\text{cm}^2/\text{s}$ .) Each model version is restarted from an 8000 year control integration with  $K_v=0.15$ , and spun up for an additional 3000-4000 years (longer for smaller  $K_v$ ) using constant pre-industrial forcing until climate and carbon cycle are in quasi-equilibrium. Initially atmospheric  $\text{CO}_2$  is fixed at 280 ppmv, but for the last ~1000 years of the spin up it is calculated interactively. Equilibrium is determined if changes in atmospheric  $\text{CO}_2$  are less than 5 ppmv per 1000 years, so that at the end of the spin up atmospheric  $\text{CO}_2$  is within  $\pm 5$  ppmv of ice core measurements of its pre-industrial value of 280 ppmv (Figure 1) for all model versions. Subsequent estimates [Crowley, 2000] of historical forcing from year 1800 to 1998 AD are applied, considering changes in solar insolation, volcanic and anthropogenic aerosol and greenhouse gases, followed by  $\text{CO}_2$  emission scenario SRES A2 until 2100 and a linear decrease of emissions to zero from year 2100 to 2300 (Figure 1). Solar, aerosol and non- $\text{CO}_2$  greenhouse gas forcings have been held constant at 1988-1998 levels for the future simulations.

## 2.2. Observations

We calculate probability densities for nine three-dimensional tracer distributions from two databases. Temperature ( $T$ ) [Locarnini et al., 2006], salinity ( $S$ ) [Antonov et al., 2006], phosphate ( $\text{PO}_4$ ) [Garcia et al., 2006b], apparent oxygen utilization ( $\text{AOU}$ ) [Garcia et al., 2006a] and preformed phosphate ( $P^*=\text{PO}_4-\text{AOU}/170$ ) are taken from the World Ocean Atlas 2005 (WOA05, data downloaded from ftp.nodc.noaa.gov/pub/data.nodc/woa/WOA05nc) and radiocarbon

( $\Delta^{14}C$ ), chlorofluorocarbon 11 (*CFC11*), dissolved inorganic carbon (*DIC*), and alkalinity (*ALK*) come from the Global Ocean Data Analysis Project (GLODAP) [Key *et al.*, 2004]. Both databases provide data on a  $1 \times 1^\circ$  grid with 33 vertical levels. The observations are averaged onto the  $1.8 \times 3.6^\circ$  model grid with 19 vertical levels. GLODAP data represent the 1990s and are compared with the decadal model mean from 1990-2000, whereas WOA05 data represent the 1950-2000 and are compared to the model mean during this period.

### 2.3. Observation Error Estimates

To quantitatively compare observations to model projections, it is necessary to have an estimate of the observation errors. The error size determines how far from the data a model can be and remain consistent with the observations. Spatially variable error estimates for the observations ( $\sigma_{oi}$ ) are available for  $\Delta^{14}C$ , *CFC*, *DIC* and *ALK* from the GLODAP data set representing errors resulting from the objective analysis (mapping) procedure used to interpolate and extrapolate observations to a global grid. Due to the sparse observations the GLODAP error estimates are horizontally correlated with a correlation length scale of 10-20°. Thus the GLODAP errors are simply averaged onto the model grid.

The WOA05 provides the standard error for each unanalyzed variable, which is the standard deviation of the mean divided by the square root of the number of observations in each grid cell. Following the recommendation in the WOA05 documentation (available at [http://www.nodc.noaa.gov/OC5/WOA05/pr\\_woa05.html](http://www.nodc.noaa.gov/OC5/WOA05/pr_woa05.html)) the error due to the objective analysis is estimated as the difference between the value of the analyzed field and the mean at each grid cell containing observations. For *T* and *S*, which have observations at almost all grid points, this error is horizontally uncorrelated. The global horizontal root mean square is calculated at each depth level, representing the (horizontally uniform but vertically varying) mapping error. This mapping error is added to the standard error to yield the spatially variable total error estimate.

For *PO<sub>4</sub>* and *AOU* the data density is too sparse to calculate an error estimate due to the mapping procedure, because the calculation can only be performed for points that include data. For this reason we do not use the analyzed fields but rather we use the unanalyzed mean (the average of the raw observations in any given  $1 \times 1^\circ$  data grid box). This limits the number of grid cells to

those containing observations. The observations are averaged onto the model grid, and model grid cells without observations are discarded in the analysis. In this case the total error of the observations is only the standard error of the mean (no mapping error). For all WOA05 variables the total errors are horizontally uncorrelated and hence they are averaged onto the model grid and divided by  $2.55 = \sqrt{3.6 \times 1.8}$  in order to account for 6.48 independent data grid boxes in one model grid cell.

## 2.4. Statistical Analysis

We assess the compatibility of different diapycnal diffusivities with observed tracer measurements using Bayesian inference to compute the relative probability of each of the eight diffusivities in our ensemble implied by each of the nine tracer fields. Two different methods are used in the model assessment. The first computes the root mean squared (RMS) error (E) for each model, including the full three-dimensional (3D) spatial fields of observations. This method neglects the correlation of the errors and requires the size of the errors to be specified. The second method considers the correlation of the errors and determines the error magnitude and bias endogeneously from the data-model residuals. However, due to computational constraints it uses only 1-dimensional data (globally horizontally averaged depth profiles). Both methods, as well as the relations between them, are described in detail below.

### 2.4.1. The 3D Method

Models that greatly differ from the observations are judged less probable than models whose deviations from the data are small. To quantify this intuition, it is necessary to mathematically specify what “small” means. We introduce an error estimate  $\sigma$  to set the scale against which data-model discrepancies are evaluated. These deviations are deemed large or small relative to the magnitude of  $\sigma$ . Observations can differ from model predictions for two reasons: model structural error, and observational/measurement error. The quality of data-model agreement depends on how large we judge these errors to be (see Sec. 3.7). However, errors can be difficult to estimate *a priori* (before seeing the observational data), especially when model structural errors are substantial. Observational errors usually can be estimated from known properties of



the measurement system (Sec. 2.3), but the size of the model error typically cannot be determined without comparing the model output to observations.

To assess model skill for each tracer  $i$ , we calculate the error-weighted mean squared error

$$\overline{E_i^2} = \overline{\left( \frac{O_i - M_i}{\sigma_i} \right)^2}. \quad (1)$$

The overbar denotes the global, volume-weighted average. Deviations of each modeled 3D tracer field  $M_i = M_i(x, y, z) = \overline{M_i} + M'_i$  from the observations  $O_i = O_i(x, y, z) = \overline{O_i} + O'_i$  are weighted by a combined error estimate ( $\sigma_i^2 = \sigma_{O_i}^2 + \sigma_{M_i}^2$ ) for the observations  $\sigma_{O_i}$  and the model  $\sigma_{M_i}$ . (The prime denotes the deviation from the global mean.) Our methods for estimating the observation and model errors are discussed in Section 3.4.1.

The models often show bias relative to the observations, so that their mean prediction differs from the mean of the observations. To distinguish between the amount of error introduced by model bias and the amount of error unrelated to bias, we also consider the bias-corrected RMS error. This error is calculated by subtracting the global mean bias  $b_i = \overline{O_i} - \overline{M_i}$ , so that the bias corrected residuals  $O_i - M_i - b_i$  have zero mean. The bias-corrected RMS error is then

$$\overline{E_i'^2} = \overline{\left( \frac{O_i - M_i - b_i}{\sigma_i} \right)^2} = \overline{\left( \frac{O'_i - M'_i}{\sigma_i} \right)^2}. \quad \text{The error } \overline{E_i'^2} \text{ excludes information about the global mean}$$

data-model misfit. Assuming the errors are independent and identically-distributed random variables, the probability density

$$L(O_i | K_v) \propto \exp\left(-\frac{1}{2} \overline{E_i^2}\right) \quad (2)$$

is the likelihood that the observations  $O_i$  could arise from the model with parameter  $K_v$ . Above,

$\overline{E_i^2} = \overline{E_i^2} \times N$  is the (volume-weighted, error-weighted) sum of squared errors, equal to the mean squared error  $\overline{E_i^2}$  times the number of data points. More precisely, assuming a known error  $\sigma$ ,

the probability in equation (2) is a normal likelihood function: the observations are assumed to be drawn from a normal distribution with mean centered on the model output ( $O \sim N(\mu = M, \sigma^2)$ ). Bayes' theorem states that the posterior probability density function (PDF) for  $K_v$  is proportional to the product of the likelihood of the observations with the prior PDF of  $K_v$ ,  $p(K_v)$ :

$$p(K_v | O_i) \propto L(O_i | K_v) \times p(K_v) . \quad (3)$$

We adopt a uniform prior PDF for  $K_v$ . If the errors in different tracers are independent of each other – which is generally *not* the case, as discussed below – likelihoods for individual tracers can be multiplied to yield the combined likelihood of all tracers,  $L(O | K_v) = \prod_i L(O_i | K_v)$ .

Probability-weighted projections for a climate variable  $T$  are obtained by averaging over the possible values of  $K_v$ ,

$$\bar{T} = \int_{K_{vmin}}^{K_{vmax}} T(K_v) \cdot p(K_v | O) dK_v , \quad (4)$$

if the PDF is defined on the interval  $[K_{vmin}, K_{vmax}]$ .

#### 2.4.2. The 1D Method

The above 3D method ignores spatial autocorrelation of the data-model residuals,  $R_i = O_i - M_i$ , which is known to lead to overconfident parameter estimates [Zellner and Tiao, 1964]. In addition, the above formulation presumes that the residual error  $\sigma$  is known, but as discussed in the previous section, it can be difficult to estimate *a priori*. Here we develop a relatively simple and computationally efficient method to estimate the combined effects of observation errors and model structural errors endogenously from the overall data-model misfit. This method is more computationally expensive than the 3D method, so we apply it to small 1D aggregated data sets instead of to the full 3D spatial fields.

When the errors are uncorrelated, only their magnitudes  $\sigma_i$  need to be specified. If the errors are correlated, the correlation between errors must be specified in addition to their magnitudes. We generalize from the error variances  $\sigma_i^2$  to an error covariance matrix  $\Sigma$ , which includes the error variances and the spatial correlations between points. In the 3D method we use the weighted sum of squared errors,  $\sum_i (O_i - M_i)^2 / \sigma_i^2$ , to quantify model skill. This error measure is not appropriate when the errors are correlated. Correlated errors effectively provide fewer independent data points than uncorrelated errors. An appropriate measure should penalize models less harshly when correlation is present, since fewer independent data are assimilated. To include correlation the sum of squared errors generalizes to a quantity involving the error covariance matrix, known as the Mahalanobis distance [Mahalanobis, 1936], which appears in the multivariate normal distribution:

$$E_i^2 = (O_i - M_i)^T \Sigma_i^{-1} (O_i - M_i). \quad (5)$$

This expression reduces to the sum of squared errors when the covariance matrix is diagonal with entries  $\sigma_i^2$ , i.e., when it contains only variances but no off-diagonal correlations. (In the remainder of this section we omit the subscript  $i$  when referring to each tracer.)

Only small covariance matrices are used here because matrix inversion is computationally expensive. To reduce the covariance matrix to a size which is feasible to invert, we consider only a 1D globally averaged spatial field of tracer data  $O_i(z)$  and  $M_i(z)$  as a function of depth  $z$ . Each field is reduced to 18 depths data points. We assume the covariance matrix  $\Sigma$  is given by a stationary squared-exponential covariance function between depths  $z_j$  and  $z_k$ ,  $\Sigma_{jk} = \sigma^2 \exp(-|z_j - z_k|^2 / \lambda^2)$ , where  $\sigma^2$  is the residual variance and  $\lambda$  is a range or correlation length parameter. Including the possibility of a constant model bias,  $b$ , the observations are assumed to be drawn from a multivariate normal likelihood centered on the bias-corrected model output ( $O \sim \text{MVN}(\mu = M + b, \Sigma)$ ).

In the 3D method, the residual error  $\sigma$ , the correlation length  $\lambda$ , and the model bias  $b$  are assumed known constants (with  $\lambda=0$ , and  $b=0$  or set to the difference in observational and model means).

These constants may differ between tracers. In the 1D method we relax these assumptions by treating the three constants as unknown statistical parameters. The full Bayesian approach, which we approximate, is to calculate a joint posterior PDF for all the uncertain parameters, including the model parameter  $K_v$  and the three statistical parameters. By Bayes' theorem, this posterior probability is proportional to the product of the likelihood of the observations with the prior probability of the parameters,

$$p(K_v, \sigma, \lambda, b | O) \propto L(O | K_v, \sigma, \lambda, b) \times p(K_v, \sigma, \lambda, b). \quad (6)$$

We are most interested in the probabilities of the different model diffusivities, not of the statistical parameters. We can obtain the posterior PDF  $p(K_v | O)$  for  $K_v$  alone by integrating the joint posterior  $p(K_v, \sigma, \lambda, b | O)$ , Eq. 6, with respect to the three statistical parameters:

$$p(K_v | O) = \iiint p(K_v, \sigma, \lambda, b | O) d\sigma d\lambda db. \quad (7)$$

However, for computational simplicity, we avoid performing this integral by fixing the statistical parameters at their best-fit values  $\sigma^*$ ,  $\lambda^*$ ,  $\beta^*$ . This gives an approximate proportionality

$$p(K_v | O) \approx p(K_v | O, \sigma^*, \lambda^*, b^*) \propto L(O | K_v, \sigma^*, \lambda^*, b^*) \times p(K_v, \sigma^*, \lambda^*, b^*). \quad (8)$$

Fixing the statistical parameters ignores their uncertainty but still accounts for the presence of model error, bias, and correlation. These quantities are estimated from the data-model misfit instead of assumed from expert prior judgement. The best estimate for  $\sigma^*$ ,  $\lambda^*$ ,  $\beta^*$  is obtained by numerically maximizing the posterior probability (Eq. 6) using a global optimization method [Storn and Price, 1997] to account for potential multimodality. Posterior maximization is analogous to maximum likelihood estimation [Lehmann and Casella, 2003], except that the likelihood is modified by prior constraints on the parameters. The statistical parameters are separately optimized for each tracer, allowing the estimated residual structure to vary between tracers. For every tracer, the parameters are also re-optimized for each member of the ensemble. In other words, the statistical parameters are allowed to depend on  $K_v$ . The logic behind this

assumption is that the model error depends on the model parameters, since poorly fitting models should have larger model error and bias. We linearly interpolate the posterior probability onto a regular grid of  $K_v$  and normalize the integral to unity to arrive at a proper probability density function.

We choose a uniform prior for the model parameter  $K_v$ . The correlation length prior is  $p(\lambda) = \text{Lognormal}(5.5, 0.5^2)$ . That is,  $\ln(\lambda)$  is normally distributed with a mean 5.5 and standard deviation 0.5. This prior puts most of its probability mass between 0 and 600 meters, excluding unphysically large correlations between the ocean surface and bottom in a globally averaged depth profile. We use a joint prior for the residual variance and bias,  $p(b/\sigma) = N(0, 0.5^2)$ . This prior is selected so the model bias for the best  $K_v$  value is assumed to be likely smaller than the residual error (i.e.,  $b/\sigma$  is near zero). This gives low prior weight to models with large biases, where “large” is quantified relative to the size of the bias-corrected error,  $\sigma$ . Exploratory analysis indicates that an improper, unbounded uniform prior for the range or bias parameters can lead to ill-conditioned covariance matrices and non-robust results for the  $K_v$  posterior distribution.

### 3. Results

#### 3.1. Global Metrics

Observed atmospheric CO<sub>2</sub> concentrations and global mean surface air temperatures are simulated roughly equally well in all model versions, irrespective of the value of  $K_v$  (Figure 1). This is also true for the ocean heat content changes, which are very similar in all simulations (Figure 2). As already concluded in *Tomassini et al.* [2007], these globally aggregated observations provide relatively poor constraints on  $K_v$ . The model suggests, however, that this situation might change in the future, because the simulations for different  $K_v$  values diverge notably during the 21<sup>st</sup> century. For example, at year 2100 differences in CO<sub>2</sub> concentrations are about 70 ppmv (Figure 1). This suggests that variations in diapycnal diffusivity alone can account for about 25% of the range in the C<sup>4</sup>MIP models. At year 2300 differences in CO<sub>2</sub> concentrations are more than 200 ppmv. Differences in projected global average surface air temperatures are 0.8°C in model year 2100 and 1°C in year 2300.

### 3.2. Influence of Diapycnal Mixing on Climate-Carbon Cycle Projections

Larger diapycnal mixing leads to faster oceanic uptake of heat and CO<sub>2</sub> in the model. Both effects tend to delay and reduce atmospheric warming. Faster CO<sub>2</sub> uptake leads to lower atmospheric CO<sub>2</sub> concentrations and thus reduced radiative forcing, whereas faster heat uptake leads to slower warming of surface waters and therefore delayed warming of surface air temperatures. We separate these two effects by comparing a simulation with weak mixing ( $K_v = 0.1$ ) forced with interactive CO<sub>2</sub> to one forced with a prescribed CO<sub>2</sub> evolution (and thus radiative forcing) taken from a run with vigorous mixing ( $K_v = 0.5$ ). The difference in surface air temperature evolution between these two simulations is due only to the effect of slower ocean heat uptake. The effect of different ocean carbon uptakes is quantified by comparing the simulation with prescribed CO<sub>2</sub> to the fully coupled run with  $K_v = 0.1$  (Figure 3). The global surface air temperature increase in the run with prescribed CO<sub>2</sub> evolution is about half way between the experiments with high and low  $K_v$ . About 55% (0.5 K) of the reduced warming of air temperatures in the high versus the low  $K_v$  simulation is explained by differences in ocean heat uptake alone, and 45% is caused by faster CO<sub>2</sub> uptake. This demonstrates that both effects, slower heat uptake and slower carbon uptake, contribute about equally to the reduced warming in the high mixing model projections.

We analyze the sensitivity of land ( $\Delta C_L$ ) and ocean ( $\Delta C_O$ ) carbon uptake until year 2100 with respect to changes in atmospheric CO<sub>2</sub> ( $\beta_L = \Delta C^u_L / \Delta C^u_A$ ;  $\beta_O = \Delta C^u_O / \Delta C^u_A$ ) and climate ( $\gamma_L = (\Delta C^c_L - \beta_L \Delta C^c_A) / \Delta T^c$ ;  $\gamma_O = (\Delta C^c_O - \beta_O \Delta C^c_A) / \Delta T^c$ ) following *Friedlingstein et al.* [2006], where  $c$  and  $u$  superscripts denote the coupled and uncoupled (constant climate) runs respectively,  $\Delta T$  is the global mean surface air temperature change and  $\Delta C_A$  is the atmospheric CO<sub>2</sub> anomaly. As expected the land sensitivities ( $\beta_L(K_v = 0.1) = \beta_L(K_v = 0.5) = 1.4$  GtC/ppm;  $\gamma_L(K_v = 0.1) = -114$  GtC/K;  $\gamma_L(K_v = 0.5) = -116$  GtC/K) are very similar between the different  $K_v$  simulations. (The C<sup>4</sup>MIP range for  $\beta_L$  is 0.2 to 2.8 GtC/ppm and for  $\gamma_L$  it is -20 to -177 GtC/K.)

However, ocean carbon uptake due to changes in atmospheric CO<sub>2</sub> alone is 30% smaller in the low mixing model ( $\beta_O(K_v = 0.1) = 1$  CtC/ppm) compared to the high mixing model ( $\beta_O(K_v = 0.5)$

= 1.4 CtC/ppm). This suggests that differences in ocean diapycnal mixing alone can explain half the range of  $\beta_O$  in the C<sup>4</sup>MIP models (0.8-1.6 GtC/ppm) and re-emphasizes the important role of diapycnal mixing on anthropogenic carbon uptake by the ocean. There are, of course, other processes that additionally determine ocean carbon uptake (under fixed climate), such as the strength of the overturning circulation and convection, mixed layer depths, and air-sea gas exchange (driven by factors such as sea ice and wind velocities).

Ocean carbon uptake decreases in the model simulations as climate warms due to increasing stratification of the upper ocean. A greater weakening of the ocean carbon sink corresponds to more negative values of  $\gamma_O$ . In the high mixing models this decrease is larger ( $\gamma_O(K_v = 0.5) = -45$  GtC/K) than in the low mixing models ( $\gamma_O(K_v = 0.1) = -31$  GtC/K). The C<sup>4</sup>MIP models range from -14 to -67 GtC/K (though it is worth noting that the  $\gamma_O$  value of -67 GtC/K is the result of a box model; the next largest C<sup>4</sup>MIP model value of  $\gamma_O$  is -46 GtC/K). At year 2100 the ocean takes up 4.8 GtC/yr in the low mixing model versus 6.2 GtC/yr in the high mixing model. Most (8 out of 11) C<sup>4</sup>MIP models lay within that range of ocean carbon uptake.

The strength of positive climate-carbon cycle feedbacks can be quantified by the feedback gain ( $g = 1 - \Delta C_A^u / \Delta C_A^c = -\alpha(\gamma_L + \gamma_O) / (1 + \beta_L + \beta_O)$ , where  $\alpha = \Delta T^c / \Delta C_A^c$  is the transient climate sensitivity) [Friedlingstein et al., 2006]. The effects of higher  $\beta_O$  and larger (negative)  $\gamma_O$  almost completely compensate each other, but due to the larger transient climate sensitivity ( $\alpha(K_v = 0.1) = 0.0060$  K/ppm versus  $\alpha(K_v = 0.5) = 0.0055$  K/ppm) there is a modest (10%) increase in gain in the low mixing model ( $g(K_v = 0.1) = 0.2$ ) compared to the high mixing model ( $g(K_v = 0.5) = 0.18$ ). The range of  $g$  in the C<sup>4</sup>MIP models is 0.04-0.31, which includes differences in both terrestrial and oceanic carbon cycle contributions to the total climate-carbon cycle feedback, in addition to different values of transient climate sensitivity. According to our analysis, while different  $K_v$  values can explain a substantial portion of the range of ocean carbon uptake between models,  $K_v$  differences can explain only a relatively small proportion of the inter-model range in net climate-carbon cycle feedback strength.

### 3.3. Influence of Isopycnal Mixing on Climate-Carbon Cycle Projections

Additional experiments with changes in along isopycnal diffusivity from 800 to 2000 m<sup>2</sup>/s show no differences in simulated atmospheric CO<sub>2</sub> or climate demonstrating that uncertainties in this parameter do not affect projections.

### 3.4. Model Assessment Using Spatially Resolved Ocean Tracer Observations

#### 3.4.1. Model and Observation Error Estimates

Assessing model skill requires an estimate of the discrepancy between observations and model predictions. The 3D method's likelihood function, Equation (2), assumes that the standard deviation of the data-model residuals ( $\sigma$ ) is known. The 1D method estimates this error from the residuals by an optimization procedure (Sec. 2.4.2). For the 3D method we choose to determine the residual error by more informal means. By definition, the residual error

$\sigma_i = \sqrt{\sigma_{O_i}^2 + \sigma_{M_i}^2}$  should be similar to the standard deviation of the residuals,  $\sigma_i \approx SD(O_i - M_i)$ .

For the 3D method we choose the model error  $\sigma_{M_i}$  such that this is the case for one of the best fitting models ( $K_v = 0.15$ ). (See Table 1 for values.) This model error is then applied to all ensemble members.

The model error estimates  $\sigma_{M_i}$  can also be interpreted as measures of model quality; they can be used for different models and are suitable for model intercomparisons. For example, for temperature and salinity, the values in the second row of Table 1 (3D data and  $\sigma_O = 0$ ) correspond to the global RMS error. They can be compared to those reported for the OCMIP models [Doney *et al.*, 2004, Table 2] and a subset of the Intergovernmental Panel on Climate Change Fourth Assessment Report (IPCC AR4) models [Schmittner *et al.*, 2005a]. The OCMIP range for 3D models without internal restoring is 0.84-2.18 K for temperature and 0.15-0.31 for salinity; for the IPCC AR4 fully coupled ocean atmosphere models it is 0.86-2.97 K for temperature and 0.20-0.38 for salinity.

We use the observational errors reviewed in Section 2.3 for the 3D method. For the 1D method we assume that the observation error is negligible compared with the model error, since the global averaging leads to very small observational errors (decreasing with  $\sim N_{eff}^{-1/2}$ , where  $N_{eff}$  is the effective number of observations). This is consistent with the 1D data-model residuals, which



show a smoothly varying structure more indicative of systematic model error than random observation noise.

With these error estimates, we evaluate the skill of each of the eight models in the ensemble using three metrics. We use the root mean squared (RMS) error introduced in Section 2.4.1, as well as the bias-corrected RMS error. We also compute the correlation between the observations and each model. A higher correlation indicates greater similarity between the model and the observations. We conduct sensitivity studies to explore how model skill varies with  $K_v$  as determined by each of the three skill measures.

In the following discussion we distinguish between tracers which are influenced by physical processes only such as  $T$ ,  $S$ ,  $\Delta^{14}C$ , and  $CFC11$ , and those tracers strongly affected by biological processes such as  $PO_4$ ,  $AOU$ ,  $P^*$ ,  $DIC$ , and  $ALK$ , since the latter also depend on the choice of uncertain biological model parameters. Biological effects on the radiocarbon distribution in the ocean are about 2 orders of magnitude smaller than the physical effects of decay and air-sea gas exchange.

The RMS and bias-corrected RMS errors,  $E$  and  $E'$ , are plotted in Figure 4 together with the correlation coefficients  $r_i = \overline{M_i O_i} / \sqrt{\text{var}(M_i) \cdot \text{var}(O_i)}$ , with the variance  $\text{var}(x) = \overline{x^2} - \bar{x}^2$ , using the full 3-dimensional data. The different tracers show different sensitivities to  $K_v$  depending on the global metric considered. When measured by the RMS error  $E$ , the model skill for the  $\Delta^{14}C$ ,  $AOU$ ,  $P^*$  and  $DIC$  tracers show the largest sensitivity to changes in  $K_v$ . Much of this sensitivity, however, is due to the model bias, as revealed by the difference between  $E$  and the bias corrected error  $E'$ . For  $S$ ,  $ALK$  and  $PO_4$  the bias is zero ( $E=E'$ ) because neither of these tracers exchanges with other climate system components in the model and hence their ocean inventories are fixed. When measured by the correlation coefficient, the model skill for the  $AOU$  and  $S$  tracers are most sensitive to variations in  $K_v$ .

Most tracers are in better agreement with the observations for small values of  $K_v$ , both for  $E$  and  $r$  as metrics. Correlation coefficients between model output and observations peak between 0.05 and 0.15 for all tracers except  $DIC$  and  $T$ , which are rather insensitive.  $AOU$ ,  $DIC$ ,  $\Delta^{14}C$  and  $P^*$

show very large biases for large values of  $K_v$ . The deep ocean is much too young ( $\Delta^{14}C$  too high), too vigorously ventilated ( $AOU$  too low), too poor in inorganic carbon and too high in preformed nutrients. Even if the bias is removed, the bias-corrected RMS error  $E'$  in  $AOU$  is still much larger for the high  $K_v$  models.  $CFC11$  and  $S$  are both moderately sensitive and show better agreement with the observations for low  $K_v$ , irrespective of the metric considered.  $PO_4$  and  $ALK$  are also moderately sensitive and show minima in RMS errors and maxima in correlation around  $K_v = 0.15$ .

### 3.5. Probabilities From the 3D Method

PDFs from the 3D method suggest that  $\Delta^{14}C$  is the most sensitive of the physical variables to changes in  $K_v$ , followed by  $CFC11$ ,  $T$  and  $S$  (Figure 5).  $\Delta^{14}C$ ,  $S$ , and  $CFC11$  show the maximum probability for small values of  $K_v$ . For  $\Delta^{14}C$  the probability for small  $K_v$  is about three times as high as that for high  $K_v$ .  $T$  shows a broad maximum for  $0.2 \leq K_v \leq 0.4$  and smallest probabilities for very high and very low values of  $K_v$ . The biological tracers (lower panel in Fig. 5) are all sensitive to variations in  $K_v$ , in particular  $AOU$ ,  $DIC$ , and  $P^*$  which are 5-10 times more likely for low than high  $K_v$ .  $ALK$  and  $PO_4$  show maxima for  $K_v$  around 0.15-0.2.

### 3.6. Probabilities From the 1D Method

Figure 6 shows PDFs for the same variables but using the 1D method. The most obvious difference is that the 1D PDFs are much sharper than those obtained with the 3D method. This might be counterintuitive, since information was lost by aggregating the data from 3D to 1D (we discuss this effect further below). The 1D method yields maxima for all tracers for  $0.01 \leq K_v \leq 0.2$ . Probabilities for  $K_v > 0.4$  are very small for all tracers. Thus the two statistical methods agree that high  $K_v$  models are less consistent with the observations than low  $K_v$  models. Both methods also exhibit similar shapes for most tracers. E.g.  $\Delta^{14}C$ ,  $S$ ,  $AOU$ ,  $DIC$  and  $P^*$  all have maxima for  $K_v < 0.2$ ,  $CFC11$ ,  $ALK$  and  $PO_4$  show maxima for  $0.1 \leq K_v \leq 0.2$ , and  $T$  shows a broad maximum for  $0.2 \leq K_v \leq 0.3$ .

### 3.7. Sensitivity Tests

We conduct four simple sensitivity analyses of the 3D method to gain some insights into the factors that influence the differences in the posterior PDFs between the 3D and 1D methods

(Figure 7). First, we test the assumption of neglecting the error of the observations by setting  $\sigma_o=0$  and re-estimating the total error  $\sigma$  (Table 1). Comparing the resulting PDFs (blue lines) with the original PDFs (black lines) shows that this effect is negligible for most tracers. Only *CFC11*,  $\Delta^{14}C$ , and *DIC* show small differences.

Second, we calculated the PDFs for 1D (horizontally averaged) data but using the 3D method as described above (red solid lines in Fig. 7). The re-estimated errors (Table 1) are much smaller than in the 3D case for all tracers, indicating that the model has considerably more skill in reproducing the horizontally averaged observations than the full 3D distributions. The resulting PDFs are therefore much sharper than in the 3D case and for most tracers they are similar to the PDFs from the 1D method (Figure 6).

Third, we evaluate the effects of correcting for spatial autocorrelation. Following *Ricciuto et al.* [2008] we remove the lag-1 autocorrelation ( $a$ ) from the 1D residuals according to:

$$\overline{E_i^2} = \overline{(R_i(z_k) - aR_i(z_{k-1}))^2}. \quad (9)$$

As expected from earlier studies [*Ricciuto et al.*, 2008; *Zellner and Tiao*, 1964] this approach to account for the autocorrelation (green lines in Fig. 7) leads to broader PDFs (compared to the red solid lines). Neglecting spatial autocorrelation typically results in overconfident parameter estimates. The fact that the PDFs are quite different emphasizes the importance of properly considering spatial autocorrelation.

Fourth, the PDFs are re-calculated for the 1D data (without subtracting autocorrelation) but using the error estimate from the 3D method with  $\sigma_o=0$  (red dashed lines in Fig. 7). Thus the difference between the red solid lines and the red dashed lines in Fig. 7 isolates the effect of different estimated  $\sigma$ . The difference between the red dashed lines and the blue lines isolates the effect of the reduced information content in the 1D versus the 3D residuals. For most tracers the PDFs are broader than those in the high  $\sigma$  cases (red solid lines) and more similar to the 3D case (blue lines). This indicates that the most important reason for the difference between the 1D and 3D methods (and the explanation for the sharper PDFs in the 1D method) is the differently

estimated  $\sigma$ . It also suggests that spatial aggregation, despite a loss of information, can help to improve the model skill, and as a consequence lead to sharper PDFs. For  $PO_4$ ,  $CFC11$ , and  $ALK$  the red dashed lines deviate substantially from the blue solid lines. This indicates an important loss of information due to the averaging. These tracers might not be suitable for the 1D method.

### 3.8. Probabilities for Multiple Tracers

Each of the tracers examined above contains different information and leads to a different PDF for  $K_v$ . Our goal, however, is to produce a single PDF combining the information from all tracers as outlined in sub-section 2.4.1.

The distribution of each tracer is influenced not only by diapycnal mixing and the large-scale ocean circulation, but also by other processes. Some tracers, such as  $T$ ,  $S$ ,  $CFC11$ ,  $\Delta^{14}C$ , and  $DIC$ , are also influenced by air-sea exchange. Thus, the model errors, and hence the PDF, for  $T$  e.g., might be influenced by model biases in ocean-atmosphere heat fluxes, which are controlled by radiative fluxes as well as sensible and latent heat fluxes. The PDF for  $S$ , on the other hand, is influenced by surface ocean water fluxes, which are determined by evaporation, precipitation and river runoff, and thus by the atmospheric hydrological cycle. Because different physical processes control heat and water fluxes it is highly unlikely that model errors in heat fluxes are correlated with errors in water fluxes. Similarly, the air-sea fluxes of carbon, radiocarbon and CFCs are presumably independent from heat and water fluxes. Thus, considering multiple tracers can possibly average out model errors in individual air-sea fluxes. If the errors in the tracer residuals are independent between tracers, a combined likelihood for all tracers can be calculated by multiplying the likelihoods of the individual tracers as described at the end of section 2.4.1.

On the other hand, if tracers are not independent multiplication of the likelihoods would lead to overconfident and possibly biased PDFs. Sinking of particulate organic matter (the soft-tissue biological pump), for instance, influences  $PO_4$ ,  $AOU$ , and  $DIC$  and thus errors in those tracers cannot be expected to be independent. An objective way to determine independence between different tracers is to examine correlations between the errors of the residuals. As shown in Table 2, the different tracers are generally not independent.  $PO_4$ ,  $AOU$ , and  $DIC$  are clearly related for

the reasons mentioned above, but other tracer residuals (such as  $T$  and  $S$ ) are also correlated, for less obvious reasons.

At this point no method that we are aware of has accounted for the cross-tracer correlation. It is highly desirable to develop such a method in the future. For the time being we calculate PDFs for different combinations of uncorrelated tracers (Figure 8). All combined PDFs show low probability for models with high mixing rates ( $K_v > 0.3$ ). The different tracer combinations do not agree well for the probability of low mixing models. Some show a distinct maximum around 0.1-0.2 and considerably lower probabilities for lower  $K_v$ , whereas others show high probabilities for the lowest diffusivities. We conclude that the observations put a firm upper limit on the diffusivities, whereas no unequivocal lower limit can be determined.

#### 4. Discussion

One issue that has not been addressed here is parameter interactions. Generally model tracer distributions are influenced by more than one parameter, each of which is uncertain. Thus, the results obtained by varying one parameter depend on the values of many other parameters. This is also true in our case, and hence the probabilities for different  $K_v$  presented here are tentative and should be regarded as a test of the methodology rather than a definitive result.

Parameter interactions might be most obvious for tracers affected by biological processes such as  $PO_4$ ,  $AOU$ ,  $P^*$ ,  $DIC$  and  $ALK$ , which are sensitive to ill-constrained biological model parameters. Surface nutrient concentrations and deep ocean  $AOU$ ,  $P^*$  and  $DIC$ , for instance, all depend strongly on the maximum growth rate of phytoplankton ( $\gamma$ ) which determines the efficiency of the biological pump. The vertical alkalinity gradient is controlled by the fixed ratio of calcium carbonate versus particulate organic carbon production ( $R_{CaCO_3/POC}$ ). These biological model parameters were tuned for a model version with  $K_v = 0.15$  ( $\gamma = 0.13 \text{ d}^{-1}$ ,  $R_{CaCO_3/POC} = 0.03$ ). Thus larger errors for those tracers in models with different  $K_v$  can be expected because the biological parameters are unadjusted. Models with  $K_v > 0.15$  therefore overestimate surface nutrient concentrations because of more intense advective and diffusive transport of nutrient rich deep waters to the surface. Similarly, models with  $K_v > 0.15$  underestimate the efficiency of the biological pump and hence the deep ocean  $AOU$  and  $DIC$ , and overestimate  $P^*$ . Thus  $\gamma$  should be

increased together with  $K_v$ . Faster rates of nutrient input into the euphotic zone, in the strong mixing models, also lead to increased primary and export production [Schmittner *et al.*, 2005b] and higher production of  $\text{CaCO}_3$ , resulting in overestimated vertical alkalinity gradients. Thus,  $R_{\text{CaCO}_3/\text{POC}}$  should be decreased as  $K_v$  is increased.

Due to computational constraints we are currently not able to retune the biological parameters for each model version with different  $K_v$ . A simple optimization of biological parameters for the model version with  $K_v = 0.5$  ( $\gamma = 0.2 \text{ d}^{-1}$ ,  $R_{\text{CaCO}_3/\text{POC}} = 0.02$ ) results in a decrease of the errors with respect to the untuned values shown in Figure 3, but the errors are still significantly larger than those of the low  $K_v$  models. Thus, the true likelihoods for the biological tracers would presumably increase for model versions with high  $K_v$ . It is highly desirable to include these known cross-parameter dependencies in a larger model ensemble in the future. Of course, tracer distributions not affected by biological parameters, such as  $\Delta^{14}\text{C}$  (radiocarbon in our model is not influenced by biological parameters) and CFCs, do not suffer from this complication. Therefore our conclusion that models with  $K_v > 0.3 \text{ cm}^2/\text{s}$  are increasingly inconsistent with observations holds true based on these tracers alone.

An outstanding question remains whether the  $\text{C}^4\text{MIP}$  model results represent the true uncertainty of our understanding of the climate-carbon cycle system. This question can be addressed only by a systematic comparison with observations. We have shown here that low values of  $K_v$  are most consistent with ocean tracer observations, and that most of the  $\text{C}^4\text{MIP}$  models fall within the range of ocean carbon uptake simulated by varying  $K_v$  values in this study. If the values for  $K_v$  were known for the different  $\text{C}^4\text{MIP}$  models, it would be possible to reject projections from models with high  $K_v$  values, or judge them as less reliable than those from models with low  $K_v$ . However, we are not aware of a published documentation of the values of  $K_v$  used by the  $\text{C}^4\text{MIP}$  models (effective diapycnal diffusivity can also contain a difficult-to-evaluate numerical component). There is an additional complication arising from different structural types of ocean models represented in  $\text{C}^4\text{MIP}$  (box models, versus 2D models, versus GCMs). In practice, therefore, it remains difficult to assign the likelihoods we have derived here directly to the  $\text{C}^4\text{MIP}$  model projections. However, we think that the methodology developed here can be used

for multi-model assessments in the future, given that spatially resolved tracer model data output is provided.

## 5. Conclusions

We have shown that uncertainties in the value of diapycnal mixing in the pelagic ocean contribute to the spread in future model projections of CO<sub>2</sub> and climate in response to anthropogenic carbon emissions. Models with low mixing lead to slower uptake of carbon and heat by the ocean, therefore contributing to higher atmospheric CO<sub>2</sub> and warmer air temperatures. These results suggest that models with large ocean vertical mixing (high  $K_v$ ) systematically underestimate future warming and CO<sub>2</sub> concentrations, thereby possibly significantly contributing to the large range in transient climate sensitivity and climate-carbon cycle feedbacks diagnosed in earlier model intercomparisons.

Globally averaged metrics such as historic changes in globally averaged surface air temperature or ocean heat content do not provide strong constraints on  $K_v$  [Tomassini *et al.*, 2007]. We show that spatially resolved physical, geochemical and biogeochemical tracer observations in the ocean can be used to reduce the uncertainty of this parameter (and, by extension, that of future climate projections). These observations provide a firm upper limit on the value of  $K_v$ , whereas the lower limit is less well constrained. Our best estimate for the background diapycnal diffusivity in the pelagic ocean is 0.05-0.2 cm<sup>2</sup>/s, in agreement with independent estimates based on dye dispersion experiments and microstructure turbulence measurements [Ledwell *et al.*, 1993; Toole *et al.*, 1994].

We have developed a Bayesian model-data fusion method that can be used to quantify and reduce the uncertainty in future climate-carbon cycle projections. Remaining issues that need more work are cross-tracer correlations, parameter interactions and the optimal degree of spatial aggregation. Resolution of the second issue is simply one of computational resources, while the first needs further development and refinement of the existing statistical methodology and theory. To resolve the third issue, the optimal degree of aggregation can presumably be determined in a sensitivity study with successively larger spatial scales of averaging. None of those issues seems insurmountable. The prospects of robust likelihood-based model assessment,

using multiple observations considering spatial and temporal autocorrelation as well as cross-tracer correlations has the potential to lead towards truly probabilistic projections of climate and the carbon cycle.

#### **Acknowledgements**

We thank Roman Tonkonojenkov, Murali Haran, Sham Bhat, Marlos Goes, Josh Dorin, and Brian Tuttle for helpful discussions. Any potential errors and omissions are, of course, ours. We are grateful for the support from Mike Eby and Andrew Weaver from the UVic model development team. Financial support from the National Science Foundation, the Canadian Foundation for Climate and Atmospheric Sciences, and the Penn State Climate Risk Management Initiative is gratefully acknowledged. Any opinions, findings and conclusions or recommendations expressed in this material are those of the authors and do not necessarily reflect the views of the funding entity.



## References

- Antonov, J., R. A. Locarnini, T. Boyer, A. V. Mishonov, and H. E. Garcia (2006), World Ocean Atlas 2005. Volume 2: Salinity, 182 pp, U.S. Government Printing Office, Washington, D.C.
- Brohan, P., J. J. Kennedy, I. Harris, S. F. B. Tett, and P. D. Jones (2006), Uncertainty estimates in regional and global observed temperature changes: A new data set from 1850, *J. Geophys. Res.*, *111*(D12), D12106, doi: 10.1029/2005JD006548.
- Bryan, F. (1987), Parameter Sensitivity of Primitive Equation Ocean General Circulation Models, *J. Phys. Oceanogr.*, *17*(7), 970-985.
- Canadell, J. G., et al. (2007), Contributions to accelerating atmospheric CO<sub>2</sub> growth from economic activity, carbon intensity, and efficiency of natural sinks, *Proceedings of the National Academy of Sciences of the United States of America*, *104*(47), 18866-18870.
- Canadell, J. G., P. Ciais, T. J. Conway, C. B. Field, C. Le Quere, R. A. Houghton, G. Marland, and M. R. Raupach (2008), Carbon budget and trends 2007, Global Carbon Project, [www.globalcarbonproject.org](http://www.globalcarbonproject.org), 26 September 2008.
- Cox, P. M., R. A. Betts, C. D. Jones, S. A. Spall, and I. J. Totterdell (2000), Acceleration of global warming due to carbon-cycle feedbacks in a coupled climate model, *Nature*, *408*(6809), 184-187.
- Crowley, T. J. (2000), Causes of climate change over the past 1000 years, *Science*, *289*(5477), 270-277.
- Domingues, C. M., J. A. Church, N. J. White, P. J. Gleckler, S. E. Wijffels, P. M. Barker, and J. R. Dunn (2008), Improved estimates of upper-ocean warming and multi-decadal sea-level rise, *Nature*, *453*(7198), 1090-1093.
- Doney, S. C., et al. (2004), Evaluating global ocean carbon models: The importance of realistic physics, *Glob. Biogeochem. Cycles*, *18*(3), GB3017, doi: 10.1029/2003GB002150.

720 Dufresne, J. L., P. Friedlingstein, M. Berthelot, L. Bopp, P. Ciais, L. Fairhead, H. Le Treut, and  
721 P. Monfray (2002), On the magnitude of positive feedback between future climate change and  
722 the carbon cycle, *Geophys. Res. Lett.*, 29(10), 1405.

723 England, M. H., and E. Maier-Reimer (2001), Using chemical tracers to assess ocean models,  
724 *Reviews in Geophysics*, 39, 29-70.

725 Friedlingstein, P., J. L. Dufresne, P. M. Cox, and P. Rayner (2003), How positive is the feedback  
726 between climate change and the carbon cycle?, *Tellus B*, 55(2), 692-700.

727 Friedlingstein, P., et al. (2006), Climate-carbon cycle feedback analysis: Results from the C4MIP  
728 model intercomparison, *J. Clim.*, 19(14), 3337-3353.

729 Garcia, H. E., R. A. Locarnini, T. P. Boyer, and J. Antonov (2006a), World Ocean Atlas 2005.  
730 Volume 4: Dissolved Oxygen, Apparent Oxygen Utilization, and Oxygen Saturation, 342 pp,  
731 U.S. Government Printing Office, Washington, D.C.

732 Garcia, H. E., R. A. Locarnini, T. P. Boyer, and J. Antonov (2006b), World Ocean Atlas 2005.  
733 Volume 4: Nutrients (phosphate, nitrate, silicate), 396 pp, U.S. Government Printing Office,  
734 Washington, D.C.

735 Gent, P. R., and J. C. McWilliams (1990), Isopycnal mixing in ocean circulation models, *J. Phys.*  
736 *Oceanogr.*, 20, 150-155.

737 Gnanadesikan, A., J. P. Dunne, R. M. Key, K. Matsumoto, J. L. Sarmiento, R. D. Slater, and P.  
738 S. Swathi (2004), Oceanic ventilation and biogeochemical cycling: Understanding the physical  
739 mechanisms that produce realistic distributions of tracers and productivity, *Glob. Biogeochem.*  
740 *Cycles*, 18(4), Gb4010.

741 Govindasamy, B., S. Thompson, A. Mirin, M. Wickett, K. Caldeira, and C. Delire (2005),  
742 Increase of carbon cycle feedback with climate sensitivity: results from a coupled climate and  
743 carbon cycle model, *Tellus B*, 57(2), 153-163.

744 Jones, C. D., P. M. Cox, R. L. H. Essery, D. L. Roberts, and M. J. Woodage (2003), Strong  
 745 carbon cycle feedbacks in a climate model with interactive CO<sub>2</sub> and sulphate aerosols, *Geophys.*  
 746 *Res. Lett.*, 30(9), 1479, doi: 10.1029/2003GL016867.

747 Joos, F., G. K. Plattner, T. F. Stocker, O. Marchal, and A. Schmittner (1999), Global warming  
 748 and marine carbon cycle feedbacks on future atmospheric CO<sub>2</sub>, *Science*, 284(5413), 464-467.

749 Joos, F., I. C. Prentice, S. Sitch, R. Meyer, G. Hooss, G. K. Plattner, S. Gerber, and K.  
 750 Hasselmann (2001), Global warming feedbacks on terrestrial carbon uptake under the  
 751 Intergovernmental Panel on Climate Change (IPCC) emission scenarios, *Glob. Biogeochem.*  
 752 *Cycles*, 15(4), 891-907.

753 Keeling, C. D., and T. P. Whorf (2005), Atmospheric CO<sub>2</sub> records from sites in the SIO air  
 754 sampling network., Carbon Dioxide Information Analysis Center, Oak Ridge National  
 755 Laboratory, U.S. Department of Energy, Oak Ridge, Tenn., U.S.A.

756 Key, R. M., et al. (2004), A global ocean carbon climatology: Results from Global Data Analysis  
 757 Project (GLODAP), *Glob. Biogeochem. Cycles*, 18(4), GB4031, doi: 10.1029/2004GB002247.

758 Le Quere, C., et al. (2007), Saturation of the Southern Ocean CO<sub>2</sub> sink due to recent climate  
 759 change, *Science*, 316(5832), 1735-1738.

760 Ledwell, J. R., A. J. Watson, and C. S. Law (1993), Evidence for Slow Mixing across the  
 761 Pycnocline from an Open-Ocean Tracer-Release Experiment, *Nature*, 364(6439), 701-703.

762 Lehmann, E. L., and G. Casella (2003), *Theory of Point Estimation*, 2 ed., Springer, New York.

763 Locarnini, R. A., A. V. Mishonov, J. Antonov, T. Boyer, and H. E. Garcia (2006), World Ocean  
 764 Atlas 2005. Volume 1: Temperature, 182 pp, U.S. Government Printing Office, Washington,  
 765 D.C.

766 Mahalanobis, P. C. (1936), On the generalized distance in statistics, *Proc. Natl. Inst. Sci. India*,  
 767 2, 49-55.

768 Matear, R. J., and A. C. Hirst (1999), Climate change feedback on the future oceanic CO<sub>2</sub>  
769 uptake, *Tellus B*, 51(3), 722-733.

770 Matsumoto, K., et al. (2004), Evaluation of ocean carbon cycle models with data-based metrics,  
771 *Geophys. Res. Lett.*, 31(7), L07303, doi: 10.1029/2003GL018970.

772 Matthews, H. D., M. Eby, A. J. Weaver, and B. J. Hawkins (2005a), Primary productivity control  
773 of simulated carbon cycle-climate feedbacks, *Geophys. Res. Lett.*, 32(14), L14708, doi:  
774 10.1029/2005GL022941.

775 Matthews, H. D., A. J. Weaver, and K. J. Meissner (2005b), Terrestrial carbon cycle dynamics  
776 under recent and future climate change, *J. Clim.*, 18(10), 1609-1628.

777 Meissner, K. J., A. J. Weaver, H. D. Matthews, and P. M. Cox (2003), The role of land surface  
778 dynamics in glacial inception: a study with the UVic Earth System Model, *Clim. Dyn.*, 21(7-8),  
779 515-537.

780 Murphy, J. M., D. M. H. Sexton, D. N. Barnett, G. S. Jones, M. J. Webb, and M. Collins (2004),  
781 Quantification of modelling uncertainties in a large ensemble of climate change simulations,  
782 *Nature*, 430(7001), 768-772.

783 Naveira Garabato, A. C., K. L. Polzin, B. A. King, K. J. Heywood, and M. Visbeck (2004),  
784 Widespread intense turbulent mixing in the Southern Ocean, *Science*, 303, 210-213.

785 Neftel, A., H. Friedli, E. Moor, H. Lötscher, H. Oeschger, U. Siegenthaler, and B. Stauffer  
786 (1994), Historical CO<sub>2</sub> record from the Siple Station ice core, Carbon Dioxide Information  
787 Analysis Center, Oak Ridge National Laboratory, U.S. Department of Energy, Oak Ridge, Tenn.,  
788 U.S.A..

789 Ricciuto, D. M., K. J. Davis, and K. Keller (2008), A Bayesian calibration of a simple carbon  
790 cycle model: The role of observations in estimating and reducing uncertainty, *Glob. Biogeochem.*  
791 *Cycles*, 22(2), GB2030, doi: 10.1029/2006GB002908.

792 Sarmiento, J. L., T. M. C. Hughes, R. J. Stouffer, and S. Manabe (1998), Simulated response of  
793 the ocean carbon cycle to anthropogenic climate warming, *Nature*, 393(6682), 245-249.

794 Schartau, M., and A. Oschlies (2003), Simultaneous data-based optimization of a 1D-ecosystem  
795 model at three locations in the North Atlantic: Part I - Method and parameter estimates, *Journal*  
796 *of Marine Research*, 61(6), 765-793.

797 Schmittner, A., M. Latif, and B. Schneider (2005a), Model projections of the North Atlantic  
798 thermohaline circulation for the 21st century assessed by observations, *Geophys. Res. Lett.*,  
799 32(23), L23710, doi: 10.1029/2005GL024368.

800 Schmittner, A., A. Oschlies, X. Giraud, M. Eby, and H. L. Simmons (2005b), A global model of  
801 the marine ecosystem for long-term simulations: Sensitivity to ocean mixing, buoyancy forcing,  
802 particle sinking, and dissolved organic matter cycling, *Glob. Biogeochem. Cycles*, 19(3),  
803 GB3004, doi: 10.1029/2004GB002283.

804 Schmittner, A., A. Oschlies, H. D. Matthews, and E. D. Galbraith (2008), Future changes in  
805 climate, ocean circulation, ecosystems and biogeochemical cycling simulated for a business-as-  
806 usual CO2 emission scenario until year 4000 AD, *Glob. Biogeochem. Cycles*, 22, GB1013,  
807 doi:10.1029/2007GB002953.

808 Simmons, H. L., S. R. Jayne, L. C. St Laurent, and A. J. Weaver (2004), Tidally driven mixing in  
809 a numerical model of the ocean general circulation, *Ocean Modelling*, 6(3-4), 245-263.

810 Stainforth, D. A., et al. (2005), Uncertainty in predictions of the climate response to rising levels  
811 of greenhouse gases, *Nature*, 433(7024), 403-406.

812 Storn, R., and K. Price (1997), Differential evolution - a simple and efficient heuristic for global  
813 optimization over continuous spaces, *Journal of Global Optimization*, 11, 341-359.

814 Tomassini, L., P. Reichert, R. Knutti, T. F. Stocker, and M. E. Borsuk (2007), Robust Bayesian  
815 uncertainty analysis of climate system properties using Markov chain Monte Carlo methods, *J.*  
816 *Clim.*, 20(7), 1239-1254.

817 Toole, J. M., K. L. Polzin, and R. W. Schmitt (1994), Estimates of Diapycnal Mixing in the  
818 Abyssal Ocean, *Science*, 264(5162), 1120-1123.

819 Weaver, A. J., et al. (2001), The UVic Earth System Climate Model: Model description,  
820 climatology, and applications to past, present and future climates, *Atmos.-Ocean*, 39(4), 361-428.

821 Zellner, A., and G. C. Tiao (1964), Bayesian Analysis of the Regression Model With  
822 Autocorrelated Errors, *J. Am. Stat. Ass.*, 59(307), 763-778.

823 Zeng, N., H. F. Qian, E. Munoz, and R. Iacono (2004), How strong is carbon cycle-climate  
824 feedback under global warming?, *Geophys. Res. Lett.*, 31(20), L20203, doi:  
825 10.1029/2004GL020904.

826

827

828

## Figure captions

**Figure 1.** Hindcasts and projections of atmospheric CO<sub>2</sub> concentration (top) and near surface air temperature (SAT) anomalies from the 1960-1990 levels (bottom) for model versions with different values of  $K_v$ . The emission scenario (SRES A2 until year 2100 and linear decrease until year 2300 afterwards) is shown as the heavy dotted line in the top panel with the scale in the bottom right corner ranging from 0-30 Gt C / yr. For reference: current (2007) levels are about 8.5 Gt C / yr [Canadell *et al.*, 2008]. The insets in the upper left region of each panel show a zoom into the hindcast period (1800-2007) including CO<sub>2</sub> observations from Mauna Loa [Keeling and Whorf, 2005] and ice cores [Neftel *et al.*, 1994] (circles) and temperature observations from the HadCRUT3 [Brohan *et al.*, 2006] dataset (black wiggly line).

**Figure 2.** Upper ocean (0-700 m) heat content changes (from year 1961) as simulated by the different model versions (lines) compared to observations (grey shading) from Domingues *et al.* [2008]. The dark grey shading denotes nine year running mean values for comparison with decadal averages plotted for the model simulations. The light gray shading shows three-year averages.

**Figure 3.** Effects of reduced ocean heat and carbon uptake on projected warming resulting from smaller vertical mixing. Solid line shows the difference in global mean surface air temperature anomaly for the run with low vertical mixing ( $K_v=0.1$ ) minus the run with high vertical mixing ( $K_v=0.5$ ) including the effects of both reduced heat and carbon uptake. Dashed line corresponds to a run with  $K_v=0.1$  but with atmospheric CO<sub>2</sub> prescribed from the simulation with  $K_v=0.5$ , thus isolating the effect of reduced heat uptake alone. The effect of reduced carbon uptake is the difference between the dashed and solid line.

**Figure 4.** Normalized RMS errors  $E$  (left),  $E'$  (center) and correlation coefficients  $r$  (right) for 3D distributions of different physical (top) and biogeochemical (bottom) tracers as a function of the diapycnal background diffusivity  $K_v$ .

**Figure 5.** Posterior PDFs using the 3D method (eq. 3) for different physical (top) and biogeochemical (bottom) tracers as a function of the diapycnal background diffusivity  $K_v$ .

**Figure 6.** Posterior PDFs using the 1D method (eq. 7) for different physical (top) and biogeochemical (bottom) tracers as a function of the diapycnal background diffusivity  $K_v$ .

**Figure 7.** Sensitivity tests. Posterior PDFs as a function of the diapycnal background diffusivity  $K_v$  for different tracers using the 3D method, but different assumptions in the statistical analysis as described in the text. Note that for many tracers the black lines are indistinguishable from and covered by the blue lines.

**Figure 8.** Posterior PDFs as a function of the diapycnal background diffusivity  $K_v$  for different combinations of uncorrelated tracer distributions using the 3D method.



**Table 1.** Estimated model error  $\sigma_M$  for different assumptions and tracers.

		<i>T</i>	<i>S</i>	$\Delta^{14}C$	<i>CFC11</i>	<i>PO<sub>4</sub></i>	<i>AOU</i>	<i>DIC</i>	<i>ALK</i>	<i>P*</i>
		(K)		(permil)	(pM)	( $\mu$ M)	(mM)	( $\mu$ M)	( $\mu$ M)	( $\mu$ M)
3D	$\sigma_O \neq 0$	0.90	0.184	0	0.240	0.202	24.8	19	13.0	0.16
	$\sigma_O = 0$	0.92	0.190	20.2	0.353	0.203	24.8	25	15.2	0.16
1D	$\sigma_O = 0$	0.24	0.079	5.85	0.05	0.064	3.7	9	6.6	0.06

**Table 2.** Cross-tracer error correlation for the 3D method in the model with  $K_v = 0.15 \text{ cm}^2/\text{s}$ .

Absolute values larger than 0.3 are shown in bold.

	<i>T</i>	<i>S</i>	$\Delta^{14}C$	<i>CFC11</i>	<i>PO<sub>4</sub></i>	<i>AOU</i>	<i>DIC</i>	<i>ALK</i>
<i>T</i>								
<i>S</i>	<b>0.48</b>							
$\Delta^{14}C$	0.26	0.03						
<i>CFC11</i>	0.01	-0.04	<b>0.39</b>					
<i>PO<sub>4</sub></i>	<b>-0.42</b>	-0.22	<b>-0.41</b>	-0.23				
<i>AOU</i>	-0.09	0.12	<b>-0.36</b>	<b>-0.40</b>	<b>0.65</b>			
<i>DIC</i>	-0.20	<b>0.31</b>	<b>0.33</b>	-0.13	<b>0.52</b>	<b>0.76</b>		
<i>ALK</i>	0.04	<b>0.54</b>	0.23	-0.07	0.12	<b>0.42</b>	<b>0.72</b>	
<i>P*</i>	<b>-0.44</b>	<b>-0.42</b>	-0.19	0.08	<b>0.69</b>	-0.08	-0.05	-0.23

Figures

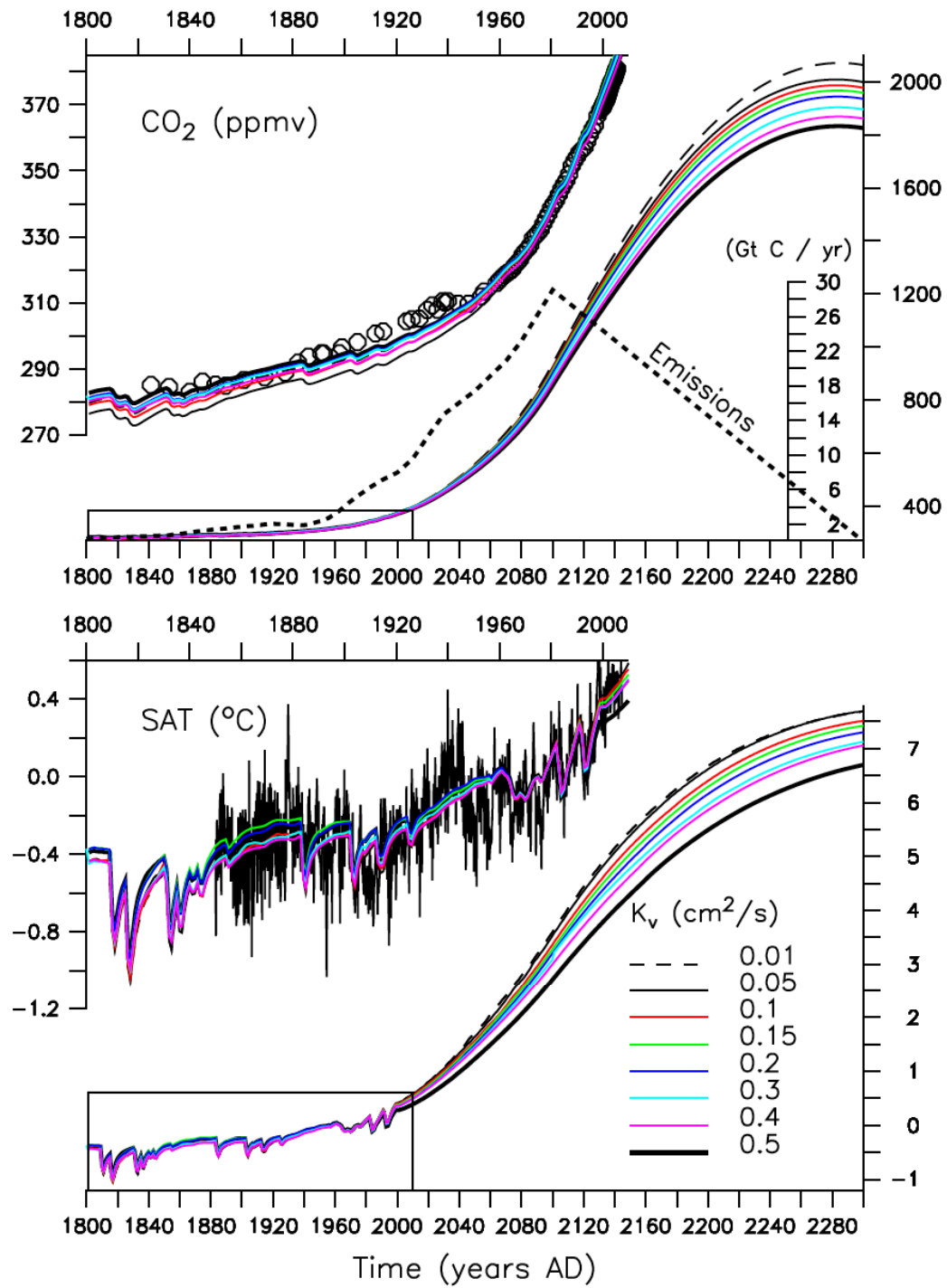


Figure 1

Ocean heat content changes, 0–700 m ( $10^{22}$  J)

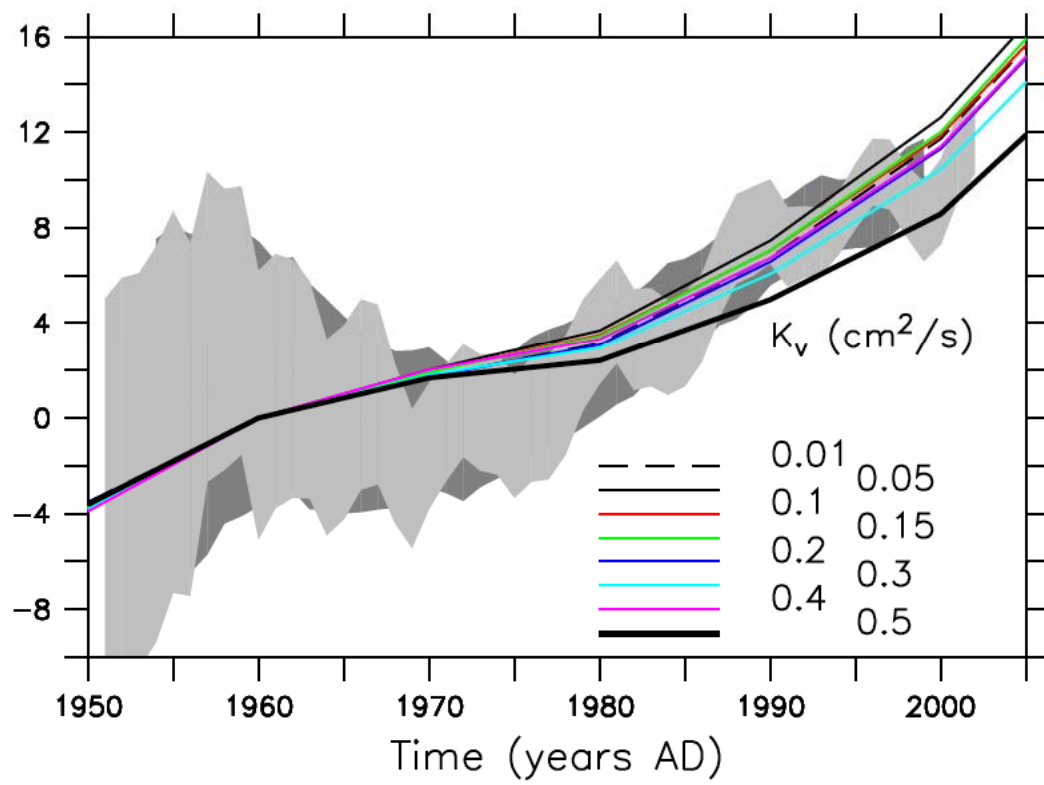
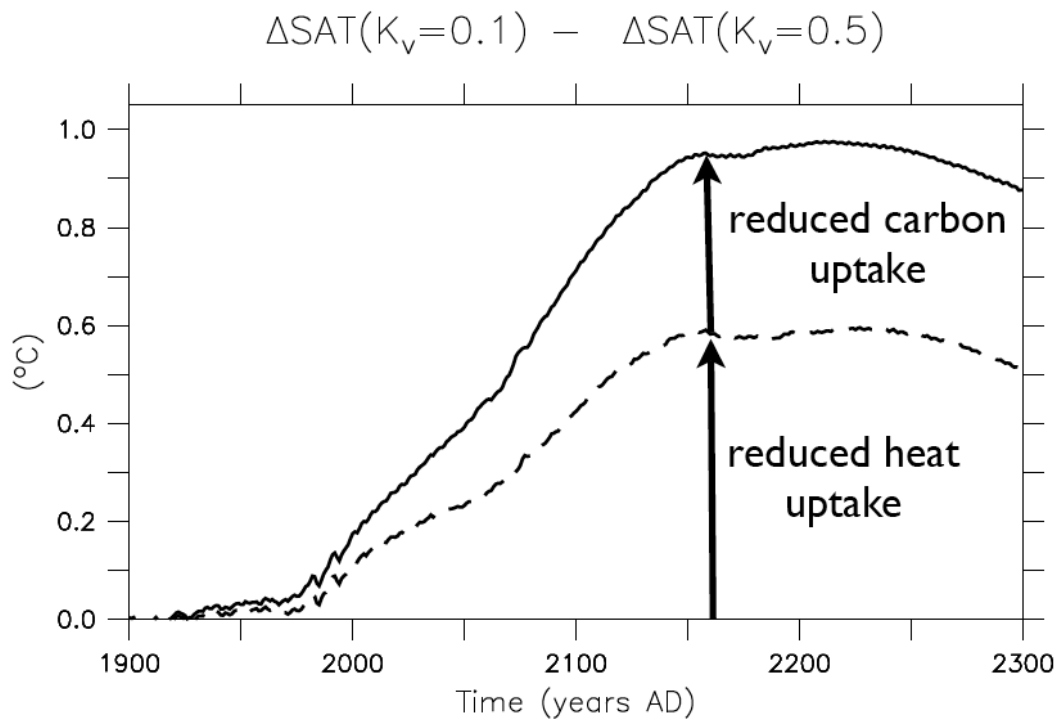


Figure 2



**Figure 3**

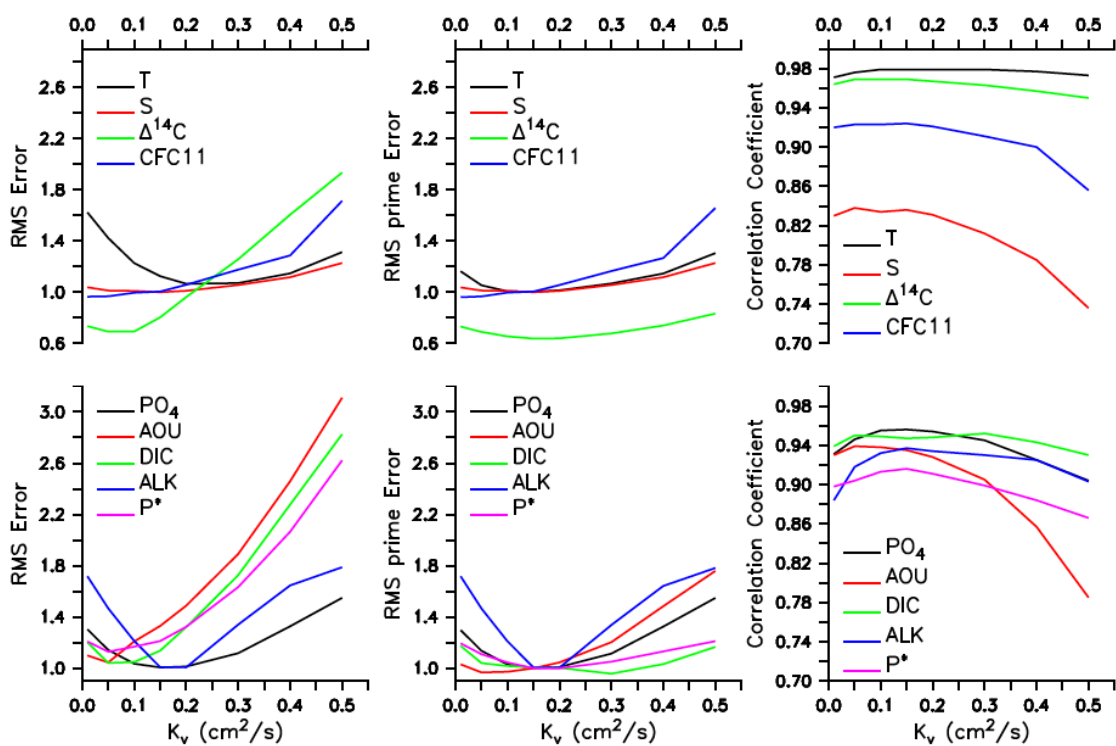


Figure 4

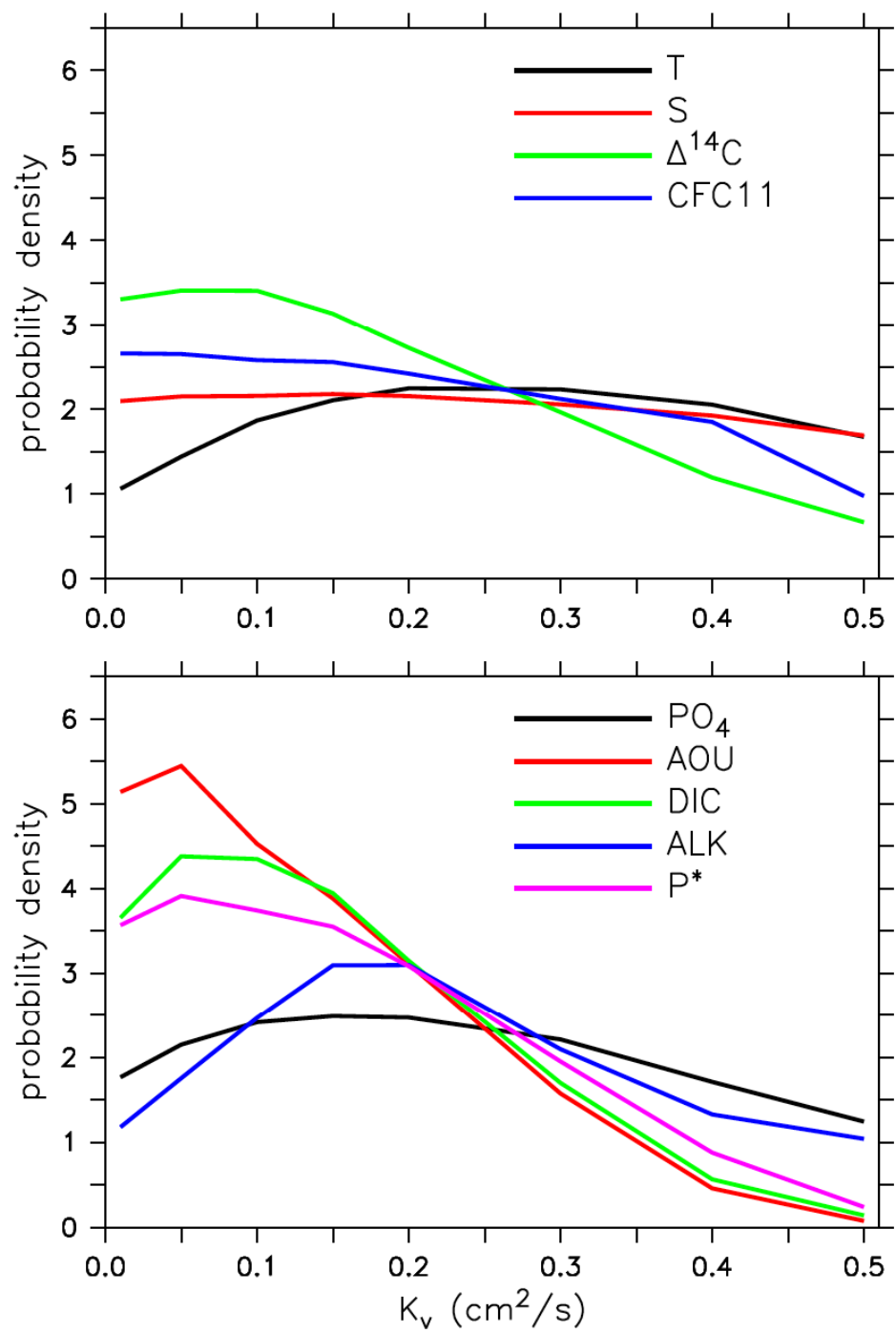


Figure 5

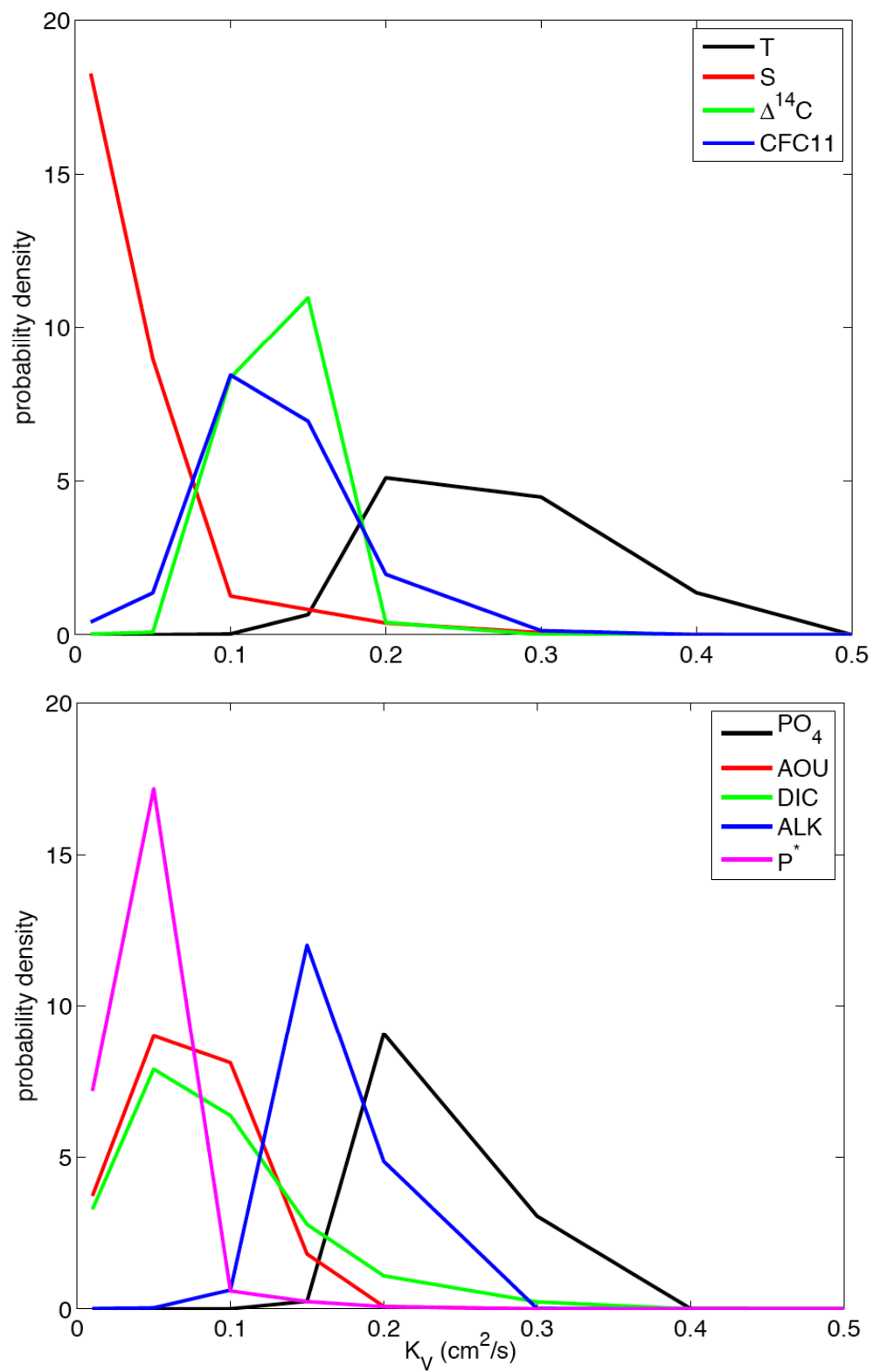


Figure 6

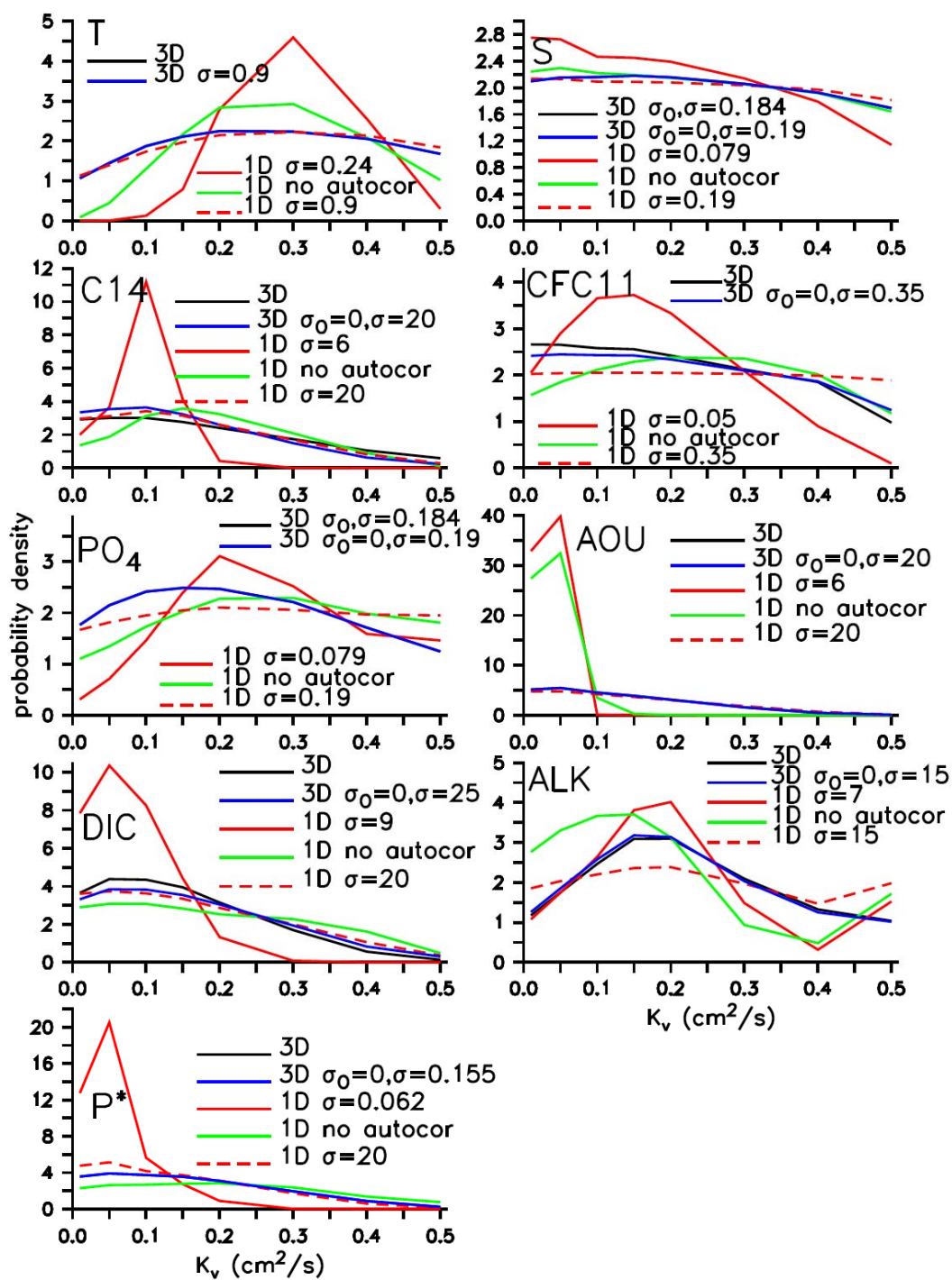


Figure 7



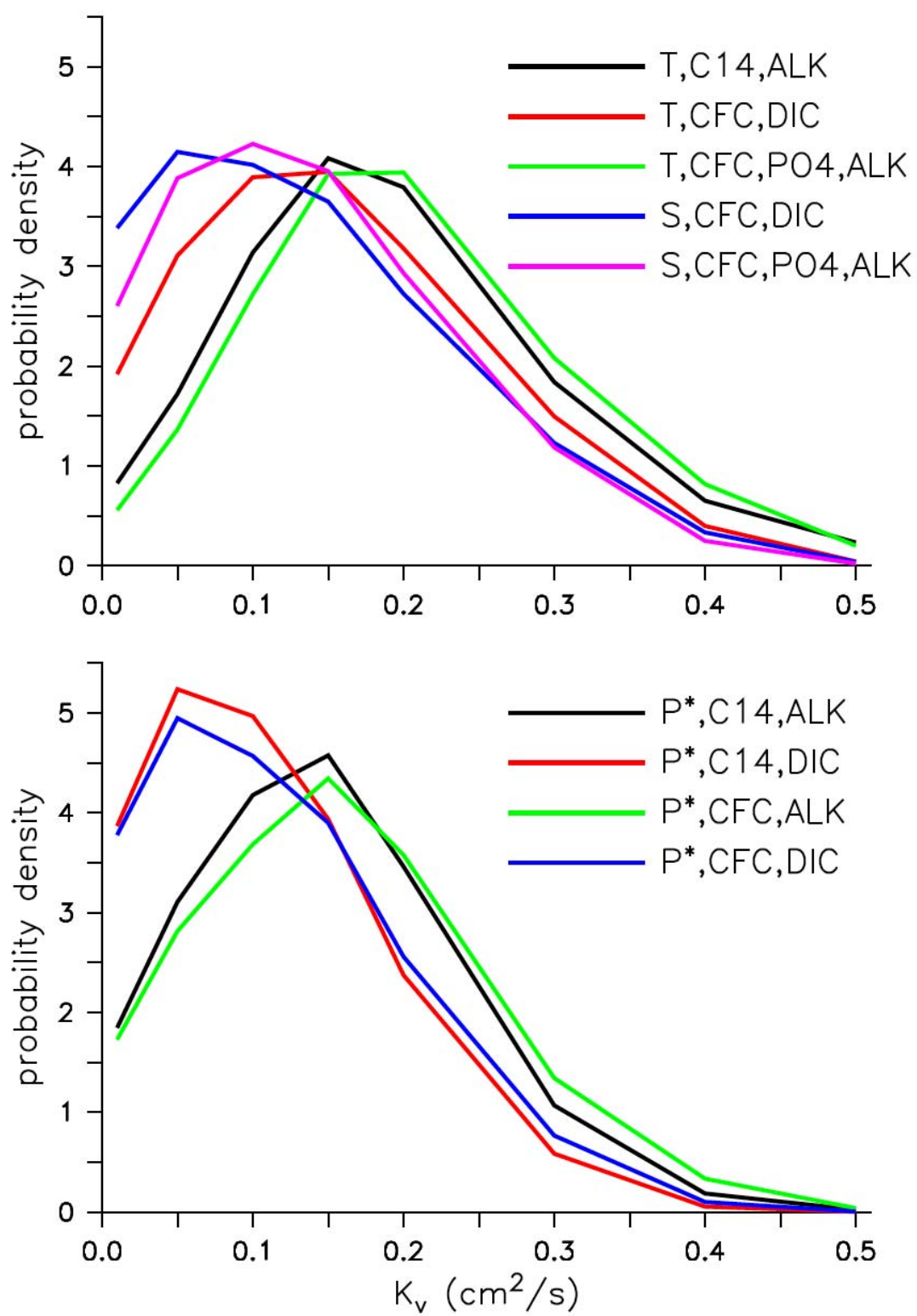


Figure 8